Research Article

Sun Yanyan, Wang Guangxin*, Li Wuhui, Wang Yaming, Satoshi Hayakawa, and Akiyoshi Osaka

Conversion of sub-μm calcium carbonate (calcite) particles to hollow hydroxyapatite agglomerates in K_2HPO_4 solutions

https://doi.org/10.1515/ntrev-2020-0070
received August 08, 2020; accepted September 04, 2020

Abstract: Sub-μm $CaCO_3$ (calcite; CC) particles were converted to calcium monohydrogenphosphate dihydrate (DCPD) and hydroxyapatite (HAp) via soaking treatments in K_2HPO_4 solutions with varied pH (3–12) and concentrations (0.1–1.5 M) at 37°C for up to 10 days. DCPD was derived from the solutions with pH ≤ 6; while hollow HAp was yielded when pH ≥ 7 in assemblies of petal-like crystallites. Results of magic angle spinning (MAS) and cross-polarization magic angle spinning (CP-MAS) NMR studies have shown that the HAp lattice has only PO_4^{2-} but no HPO_4^{2-} at B (phosphate) sites. Trace amounts of CO_3^{2-} have occupied both A (OH) and B (PO_4) sites, and H_2O is adsorbed on surface crystallites. The primary crystallite size of HAp derived from Scherrer equation increases quickly in a 12 h period and becomes gradually stable afterward. Samples of particles soaked within 3 h in a temperature range of 20–80°C were analyzed by X-ray diffraction. It is shown that the rate constant of 1 M solution is about an order of magnitude greater than that of 0.1 M solution and the apparent activation energy is 33 kJ/mol. In this work, the conversion of CC to HAp can be quantitatively controlled to solve the problem of slow degradation of HAp.

* **Corresponding author: Wang Guangxin,** Department of Materials Science and Engineering, Henan University of Science and Technology, Luoyang, Henan Province, 471023, China, e-mail: wgx58@126.com
Sun Yanyan, Li Wuhui, Wang Yaming: Department of Materials Science and Engineering, Henan University of Science and Technology, Luoyang, Henan Province, 471023, China
Satoshi Hayakawa: Graduate School of Interdisciplinary Science and Engineering in Health Systems, Okayama University, Tsushima, Okayama, 700-8530, Japan
Akiyoshi Osaka: Department of Materials Science and Engineering, Henan University of Science and Technology, Luoyang, Henan Province, 471023, China; Faculty of Engineering, Okayama University, Tsushima, Okayama, 700-8530, Japan

Keywords: calcium carbonate, hydroxyapatite, potassium monohydrogen phosphate, hollow particles, kinetic analysis, NMR

1 Introduction

Calcium carbonate (CC) is considered to be a potential bone repair material, because it can be converted to hydroxyapatite (HAp) when soaked in phosphate solutions [1–6]. The conversion process is controlled by temperature, concentration and pH value of phosphate solution. Several authors were successful in their efforts to convert CC to HAp. For example, Xia et al. [1] hydrothermally treated mixtures of CC and $(NH_4)_2HPO_4$ to prepare hollow HAp spheres. Ruffini et al. [2] applied hydrothermal procedure to convert wood-derived CC (calcite) to HAp. Minh et al. [3] soaked CC particles in H_3PO_4 solutions of varied concentrations at 80°C and found that the conversion reaction was slow and incomplete even after 168 h. Engin and Girgin [4] used H_3PO_4–H_2O–ethanol solution system for the conversion of CC at 80°C and attained calcium phosphate (Ca-P) products with a high carbonate content of 8.5%. Verwilghen et al. [5] soaked CC in $(NH_4)_2HPO_4$ solution of pH 8.05 at 60°C and observed CO_2 evolution as well as HAp formation. Portela da Silva et al. [6] derived HAp from stoichiometric mixtures of CC particles and $NH_4H_2PO_4$ solution of pH > 7 at 25°C. They found the precipitation of calcium monohydrogenphosphate dihydrate ($CaHPO_4{\cdot}2H_2O$; DCPD) in the course of the reaction, despite that Pourbaix [7] suggesting that HAp was most stable among several Ca-P phases in the range 6 < pH < 13. It is known that pH decides the chemical state of phosphate ions. They can be $H_2PO_4^-$, HPO_4^{2-}, or PO_4^{3-} [8]. Natural $CaCO_3$ of a porous framework from coral can also be a source of apatite. For example, Sethmann et al. [9] prepared macroporous apatite

ceramics via a hydrothermal treatment of aragonite coral skeletons.

Fujita et al. investigated the factors influencing the conversion of lithium calcium borate glass to HAp in dilute K_2HPO_4 solutions [10]. According to the Pourbaix diagrams [8], the ratio of $[H_2PO_4^-]/[HPO_4^{2-}]$ and $[HPO_4^{2-}]/[PO_4^{3-}]$ is 1 at pH 7.19 and 12.03, respectively. When HAp is precipitated in an aqueous solution ($6 < pH < 12$) containing an alkali hydrogen phosphate (R_2HPO_4; R = Na or K) and a calcium salt, the pH value of the solution decreases due to the consumption of OH^- ions,

$$5Ca^{2+} + 3HPO_4^{2-} + 4OH^- \rightarrow Ca_5(PO_4)_3(OH) + 3H_2O \quad (1)$$

Here stoichiometric HAp precipitation is assumed for simplicity though Ca-deficient phases will be commonly formed. The pH value of phosphate solution naturally determines the precipitated Ca-P phases [7]. Moreover, carbonate ions in CC take different forms, either HCO_3^- or CO_3^{2-}, depending on the pH of the system. Therefore, the regulation of pH value plays a key role.

Further studies tried to apply the abovementioned conversion reactions to repair bones. Fujita et al. [10] reported that CC induced an apatite layer on CC particle surface *in vitro*. Neo et al. [11] observed a direct contact between CC implants and surrounding bone tissues. Interestingly, however, neither apatite layer nor continuity between CC and bone was observed *in vivo* experiment [11]. That is, superficially, CC would not be converted to apatite *in vivo*, in contrast to the *in vitro* cases. According to the classic bioactivity theories, such an apatite layer is formed on the surface of bioactive materials [12–16] when they are in contact with human plasma or artificial aqueous solutions, mimicking the plasma and is called simulated body fluid (SBF) [14,16]. The bonding between CC and living bone without an intervening apatite layer was interpreted as a rapid biodegradation or bioresorption of CC under body conditions [11]. Kotani et al. reported a similar *in vivo* apatite-free bone-bonding behavior of β-tricalcium phosphate (β-TCP) [17], whereas Fu et al. confirmed no *in vitro* apatite layer on β-TCP in SBF [18]. An important aspect of HAp or HCA is that bioresorption is slower than TCP. Therefore, CC bone repairs blocks, and 3-D printed porous bodies or granules should be improved with regard to their usefulness when the *in vivo* biodegradation rate is adjusted by partial or full conversion to HAp or HCA before implantation.

Although a lot of knowledge has been gained regarding the conversion of CC to HAp, it is necessary to quantitatively control the conversion of CC into HAp. For bone repairs, partial conversion to HAp or conversion to DCPD may be beneficial. In order to meet such demands, this study was conducted as a systematic study to learn how factors such as pH and phosphate concentration affect the conversion of CC to DCPD or HAp.

2 Materials and methods

Figure 1 shows an SEM image of the as-received CC particles supplied by Shiraishi Kogyo Kaisha (Osaka, Japan). It can be seen that the particles are smaller than 1 μm, with most of them being around 0.4 μm. They were soaked in K_2HPO_4 solutions of four different concentrations (0.1, 0.15, 1, and 1.5 M (M = mol/L)). The pH values of the solutions were adjusted to 3.0, 5.0, 6.0, 7.0, 10.0, and 12.0 with 0.1 M HCl and KOH. All chemicals used in this study were of reagent grade and supplied by Kaitong Chemical Reagent Corporation, Tianjin, China. CC particles (0.5 g; 5 mmol) were dispersed into phosphate solutions (20 mL) held in 50 mL polystyrene bottles with tight caps. The liquid to solid ratio was set to 0.5 g/20 mL throughout this study. Bottles were kept still in an electric oven at 37°C for up to 10 days. After the soaking procedure, the CC particles were gently rinsed with distilled water for at least three times. They were then placed in glass Petri dishes with a loose cover and dried in an electric oven at 60°C for 12 h. Each experiment was repeated three times.

Dry powders were sputter coated with Au to observe their morphology in SEM (JSM-7800F; JEOL, Tokyo, Japan) operated at a 5 kV acceleration voltage. Crystal

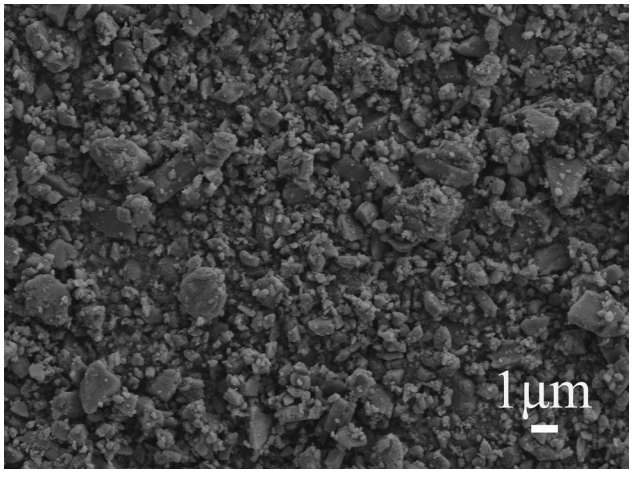

Figure 1: As-received CC (calcite) particles.

phases were identified with a X-ray diffraction (XRD) machine (Cu Kα; λ = 0.1542 nm, D8 ADVANCE; Bruker, Berlin, Germany), where the XRD profiles were taken at 8°–70° in θ–2θ mode with a scanning step of 0.02° (2θ) and a holding time of 0.2 s. X-ray area intensities of some diffraction peaks were obtained using a software equipped in the XRD machine. Local structures of ^{1}H, ^{31}P, and ^{13}C nuclei in some conversion products were examined by MAS-NMR spectroscopy (Agilent DD2 500 MHz NMR spectrometer; Agilent Technologies, Santa Clara, CA, USA), with the spinning frequency of ZrO_2 sample rotors being set to be 15 kHz for all measurements at 11.74 T. The resonance frequencies of ^{1}H, ^{31}P, and ^{13}C were 499.8, 202.3, and 125.6 MHz, respectively. The direct-polarization MAS spectra of ^{1}H, ^{31}P, and ^{13}C and also the $^{1}H \rightarrow {}^{31}P$ and $^{1}H \rightarrow {}^{13}C$ CP MAS spectra were recorded. For the ^{1}H MAS experiments, the $\pi/2$ pulse length was 2.3 μs with a 5 s recycle delay. For ^{31}P, the $\pi/4$ pulse length was 1.4 μs with a 120 s recycle delay. The contact time for $^{1}H \rightarrow {}^{31}P$ CP-MAS experiments was either 1 or 10 ms. The signals of $^{1}H \rightarrow {}^{31}P$ CP-MAS were acquired from 40 to 4,220 pulses, and 10,000–19,600 pulses were used in $^{1}H \rightarrow {}^{13}C$ CP-MAS. The chemical shift δ was obtained by external secondary references, i.e., $NH_4H_2PO_4$ for ^{31}P and adamantane for ^{1}H and ^{13}C; whereas NMR profiles were displayed with δ, which is standardized with standard reference materials of 80% H_3PO_4 and $Si(CH_3)_4$. The as-acquired NMR signals involved the signal originated from the rotor, and the NMR spectra presented in this article were based on the net signals after reducing the rotor signals. The NMR spectroscopy was used in this study to primarily examine the presence of HPO_4 and CO_3 in HAp lattice. The study was not intended to discuss peak assignments in detail.

3 Results

3.1 Effects of solution pH

Figure 2 shows the XRD profiles of CC particles soaked in 1 M K_2HPO_4 of different pH values (pH 3–12) for 3 days at 37°C. It can be seen in Figure 2 that soaking in solutions of pH ≤ 6 yielded only DCPD or brushite. But only HAp precipitated when the pH of the solutions was ≥ 7. According to ICDD 09-0432 and 09-0077, a set of sharp diffractions at 11.7°, 21.0°, 23.5°, and 29.35° and all other smaller peaks were assigned to DCPD for samples soaked in solutions of pH ≤ 6, and all diffractions in the top

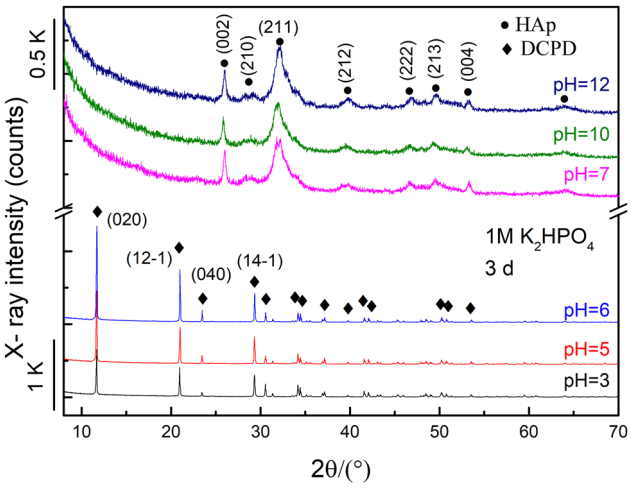

Figure 2: The XRD profiles of the conversion products after CC being soaked in 1 M K_2HPO_4 with varied pH 3–12 for 3 days at 37°C.

three profiles were assigned to HAp. Moreover, the XRD peaks of DCPD are sharper and stronger than those of HAp. This indicates that HAp was precipitated with lower crystallinity. Its primary crystallites may have smaller sizes. Such a pH-dependent precipitation of DCPD and HAp is consistent with the stability diagram for calcium phosphates proposed by Pourbaix [7]. In addition, Figure 2 demonstrates that the conversion reaction was complete within 3 days, even in solution of pH 7.

SEM images in Figure 3 show that particle morphology depends on the pH of phosphate solutions. The images in the upper raw are for acidic solutions (pH 3–6), showing agglomerations of rectangular needle-shaped crystallites with widths of ~5 μm and lengths of ~50 μm. They were DCPD according to the XRD profiles in Figure 2. The DCPD crystallites look as if they have grown radially outward. Many smaller pieces were also present in a similar shape. At pH 6, the radial growth was almost lost, and randomly oriented block-like pieces were assembled. Larger crystallites were accompanied by small chunks on their surface, as shown in insert image. When the pH ≥ 7, HAp appeared and the morphology drastically changed to agglomeration of petal-like crystallites (Figure 3d–f). In addition, some HAp agglomerates were hollow, in agreement with Figure 5(c and d) presented later. The size of agglomerates and petal-like components were reduced with increasing solution pH values. Agglomerates formed at pH 7 were about 5 μm in diameter. They consist of petals of about 0.6 μm in size. As the pH increases from 10 to 12, agglomerates' diameter decreases from 1.5 μm (pH 10) to ~1 μm (pH 12), while the petal size decreases from ~0.25 μm (pH 10) to < 0.1 μm (pH 12).

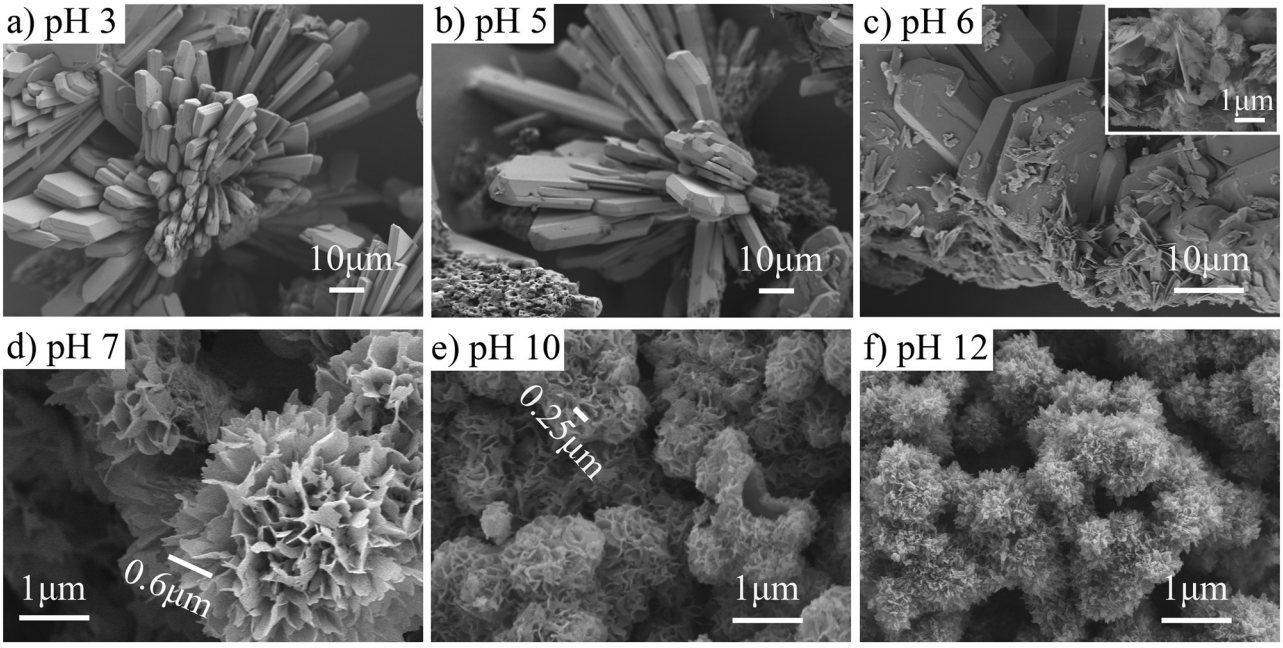

Figure 3: SEM images of the conversion products after CC being soaked in 1 M K_2HPO_4 with varied pH 3–12 for 3 days at 37°C. (a) pH = 3, (b) pH = 5, (c) pH = 6, (d) pH = 7, (e) pH = 10, and (f) pH = 12. The inset image for (c) pH 6 represents the morphology of the chunks on a larger crystal. Note the difference in magnification for the upper (bar: 10 μm) and bottom raw (bar: 1 μm) images.

An interesting observation is that the solution of pH 7 generated some bubbles, with many being found on the container wall. This implies a CO_2 generation process. In addition, the solution pH changed a little. For a solution of initial pH 7, it reached pH 8–9 in the final stage. Solutions of initial pH 10 and 12 showed a slight decrease in pH to ~10 and 11–12, respectively.

3.2 Effects of phosphate concentration

Figure 4 demonstrates XRD profiles of CC particles after being soaked in 1.5, 1.0, 0.15, and 0.1 M K_2HPO_4 at 37°C for 3 days. The initial pH of these four solutions was adjusted to 10. All XRD peaks in Figure 4 were assignable to HAp (1.5 and 1 M) and CC with a trace of HAp (0.15 and 0.1 M), and no other phases were detected. Most peaks were indexed according to ICDD 86-0174 (calcite) and ICDD 09-0432 (HAp). Sharp diffractions of CC mean that it was well crystallized, while noisy and rather broad diffractions of HAp indicate their lower crystallinity or smaller primary crystallites. This is similar to the results already found in Figure 2. With increasing phosphate concentration, the diffraction intensities of CC decreased slightly, whereas those of HAp increased a little. The absence of CC peaks for powders soaked in 1.5 and 1.0 M solutions indicates a full conversion of CC to HAp within 3 days.

SEM images in Figure 5 demonstrate surface morphologies of particles after being soaked at 37°C for 3 days in four different K_2HPO_4 solutions of initial pH 10 ((a) 0.1 M, (b) 0.15 M, (c) 1 M, and (d) 1.5 M). All particle surfaces were fully covered by fine floret or petal-like crystallites, which were identified as HAp by XRD analysis (see Figure 4). Morphologies shown in Figure 5

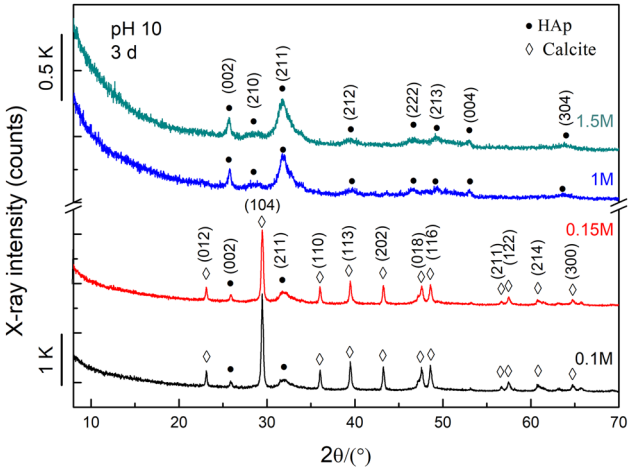

Figure 4: The XRD profiles of CC powders after being soaked in 0.1–1.5 M K_2HPO_4 solution (pH 10) at 37°C for 3 days.

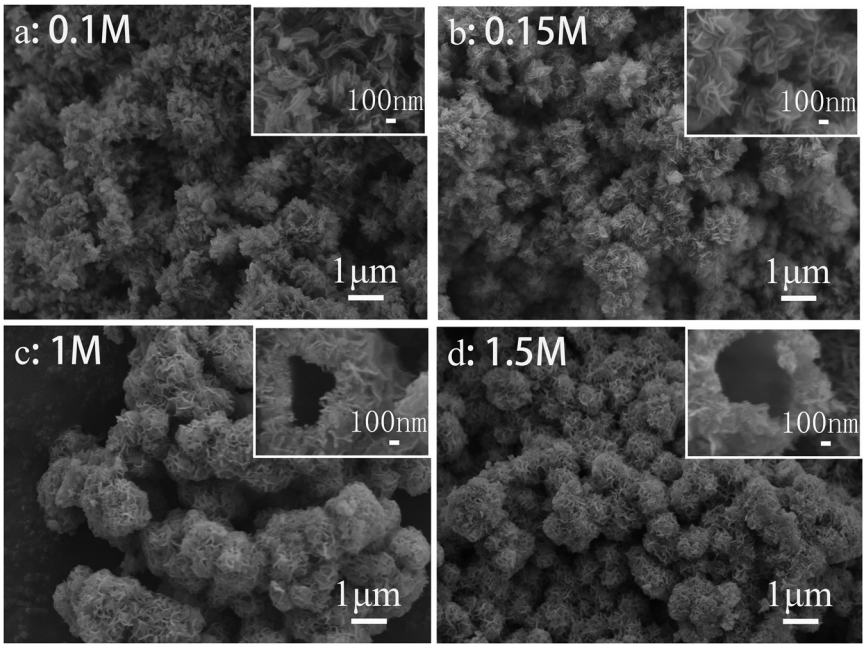

Figure 5: SEM images of hollow HAp crystallites formed on CC particles when soaked for 3 days in K_2HPO_4 solution of varied concentrations (a) 0.1 M, (b) 0.15 M, (c) 1 M, and (d) 1.5 M, pH 10, 37°C. The inserts are close-up images. W/V ratio = 0.5 g/20 mL. Bar: 1 μm (inset: 0.1 μm).

are very similar to that of HAp spontaneously deposited on the surfaces of bioactive materials [13–17]. In addition, a few hollow agglomerations of crystallites can be seen in Figure 5c and d. The agglomerate size seems to be influenced by phosphate concentration. Most agglomerates have a size of around 1 μm, which is larger than the CC particles. But the largest agglomerates of about 2 μm were seen in experiment with 1 M solution (Figure 5c). The size of the petal-like crystallites is too small to be accurately measured.

3.3 Effects of soaking time

3.3.1 Growth of HAp

Figure 6 shows the XRD profiles of samples soaked in 1 M K_2HPO_4 (pH 10) for a time range from 1 h to 240 h (10 days). It can be seen from Figure 6 that the XRD peak intensity of CC decreased. Yet, a tiny (104) peak was detected at ~29° indicating that a trace of CC still remained after being soaked for 1 day. An appearance of (002) and (211) diffraction peaks at 26° and 32°, respectively, implies that CC to HAp conversion took place within 1 h. Within 2 days, the CC was almost fully converted to HAp, leaving only a trace of the (104) peak. Within 3 days, the CC peaks disappeared completely and only HAp peaks were seen. SEM images in Figure 7 demonstrate the surface morphologies of samples soaked for (a) 1 h, (b) 2 h, and (c) 7 h. The flower-like crystals were deposited after CC being soaked for 1 h, while soaking for 2 h was sufficient for particle surfaces to be fully covered with crystallites. No apparent difference exists for morphologies of the three samples (Figure 7(a–c)).

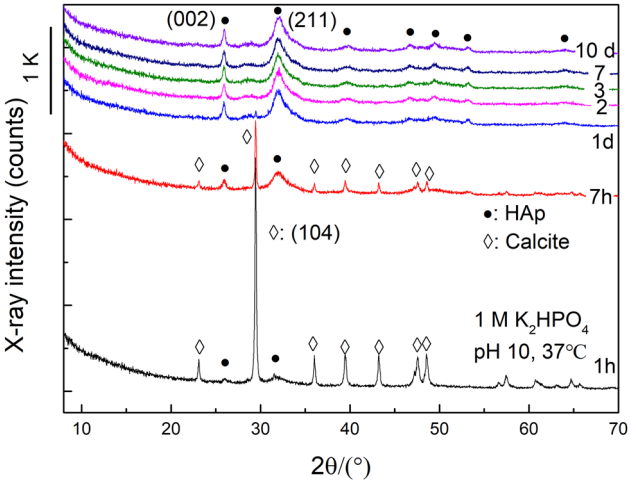

Figure 6: The XRD profiles showing effects of soaking period *t* (h) on CC to HAp conversion in a 1 M K_2HPO_4 solution of an initial pH 10 at 37°C. •: HAp; ◇: CC (calcite).

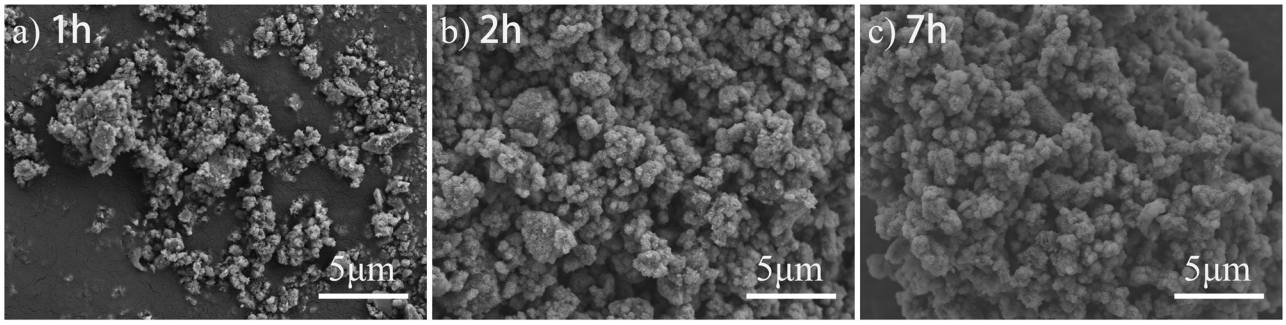

Figure 7: Surface microstructure of CC particles after being soaked in 1 M K_2HPO_4 of pH 10 for varied soaking period at 37°C. (a) 1 h, (b) 2 h, and (c) 7 h. Bar: 5 μm.

3.3.2 HAp growth rate

A XRD technique known as an internal standard method is commonly taken for deriving the volume fraction of a component phase in a mixture [19]. In this study, (104) diffraction peak of residual CC was utilized to represent the volume fraction of HAp. This peak was sharp and distinct and showed no overlapping with any other diffraction peaks of HAp. The seemingly strongest and broad peak at 31°, indexed at 211, is actually an envelope of three lines of (211), (112), and (300) planes. Kallaste and Nemliher [20] deconvoluted (separated) into those component lines. Yet, the present 211 diffraction would not deserve such deconvolution due to its intensity and sharpness.

The integrated area intensity of the (104) diffraction peak of CC was derived from diffraction profiles using an application installed on the XRD machine and then the intensity ratio $I(t)/I_0$ was calculated. Here $I(t)$ and I_0 are intensities for soaking t (h) and 0 h, respectively. In Figure 8, $I(t)/I_0$ was plotted as a function of t (h) for two soaking conditions: (a) 1 M K_2HPO_4 at 37°C, with varying pH of 7, 10, and 12; (b) different K_2HPO_4 concentrations (0.1–1.5 M) at 37°C and an initial pH 10. Again, the solid to liquid ratio was kept at 0.5 g/20 mL. From Figure 8(a), it can be seen that the conversion proceeded in three stages. In stage I (t < 3 h), CC was converted so rapidly that more than half the amount of CC, even ~80% for pH 10 and pH 12, was consumed for the conversion reaction. In stage I_{tr} (3 h < t < 12 h), a transition state, $I(t)/I_0$ decreased more slowly compared to that in stage I. In stage II (12 h < t), the conversion is almost completed within 24 h (1d). $I(t)/I_0$ decreased in all stages in the order of pH 10, pH 7, and pH 12. This is somehow surprising because the thermodynamic stability of HAp should decrease almost proportionally to pH [7]. Very similar changes were observed in Figure 8(b); in 1 and 1.5 M solutions. One-half amount of CC was exhausted within the initial stage (t < 3 h), and the reaction was completed within 24 h (1 day). Thus, the reaction process can also be divided into stages I, I_{tr}, and II as in Figure 8(a). For 0.1 and 0.15 M solutions, the decrease in $I(t)/I_0$ was very slow for t > 3 h, and it showed a very little change after 12 h, which may be due to insufficient supply of phosphate ions. Indeed, with a solid to liquid ratio of 0.5 g/20 mL, both 0.1 and 0.15 M solutions contained less amount of HPO_4^{2-} than what was necessary for a full conversion.

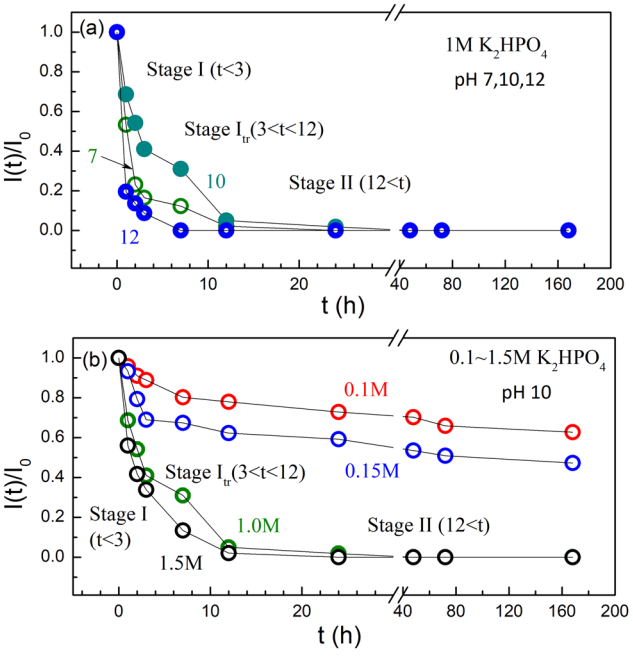

Figure 8: The XRD intensity ratio $I(t)/I_0$ as a function of t (h), showing the effects of (a) pH and (b) K_2HPO_4 concentration. Soaking temperature = 37°C.

3.4 ^{31}P, ^{1}H, and ^{13}C in DCPD and HAp

3.4.1 Assignments

The present HAp converted from CC might involve HPO_4^{2-} and CO_3^{2-} ions in the lattice because HAp from wet chemical routes is prone to be Ca deficient. It is known that bone minerals involve carbonated hydroxyapatite (HCA) [21]. The XRD technique may not have the ability to detect their presence in a low level. Therefore, MAS and CP-MAS NMR spectroscopy were applied to clarify the chemical environments around ^{1}H, ^{31}P, and ^{13}C nuclei in three representative samples S1, S2, and S3. Table 1 lists their soaking conditions as well as the NMR procedures. The chemical shift is presented in δ (ppm) as convention: a deshielded nucleus exhibits a decrease in δ or a downfield (low field) shift, while an increase in δ indicates that a shielded nucleus is characterized by an upfield (high field) shift. Figure 9(a–c) illustrate ^{31}P MAS and CP-MAS spectra and ^{1}H MAS NMR spectra of the designated samples. Figure 9(d) indicates a ^{13}C CP-MAS spectrum of HAp: S3. Peak assignment is based on the results previously selected referencing on Ca-Ps [22,23,24–33,34,35], such as anhydrous dicalcium phosphate (DCPA or monetite) [24,26,31], DCPD [24,31,32], TCP [31,32], amorphous Ca-P [30], octacalcium phosphate (OCP) [22,28,32], and HAp [22,23,24,25,27,30,33,34,35]. The peak assignments of bones or other living systems were ruled out from the reference because those minerals were not well defined in structure and chemical composition. Table 2 summarizes the chemical shifts $\delta(^{1}H)$ and $\delta(^{31}P)$ observed in the present study as well as those from the above-mentioned references.

3.4.2 ^{31}P spectra

Strong ^{31}P peaks of HAp: S1 and DCPD: S2 in Figure 9(a and b) are located at 3.07 and 1.40 ppm. They are doubtlessly attributed to the lattices PO_4^{3-} of HAp and HPO_4^{2-} of DCPD. Both MAS and CP-MAS ^{31}P spectra of HAp (Figure 9(a)) are accompanied by a sharp but weak signal at 1.0 ppm. None of the references clearly noticed this peak [22–25,27,30,33–35]. Jarlbring et al. [25] proposed a peak of ^{31}P at 0.8 ppm, which originated from a protonated orthophosphate (H_xPO_4) ion on a surface site of fluorapatite ($Ca_5(PO_4)_3F$). If this 1.0 ppm peak of ^{31}P would be assigned to a surface HPO_4 group of HAp, a sharp but weak peak should also appear around 10 ppm due to OH of HPO_4 in a ^{1}H spectrum of HAp. Jarlbring et al. [25] did not present the ^{1}H spectra of their samples. This study could not detect such a 10 ppm peak of ^{1}H in that range as shown later in Section 3.4.3. Thus, the 1.0 ppm peak was denoted unassigned in Table 1. Figure 9(b) of DCPD: S2 shows additional minor ^{31}P signals at −0.3 and ~3.5 ppm. The possibility of assigning the −0.3 ppm peak to the lattice HPO_4 of DCPA was ruled out. According to Yun et al., this peak should be accompanied by a much stronger ^{31}P peak at −1.5 ppm. The weak humps around 3.5 ppm consisted of triplet-like peaks at 3.1, 3.4, and 4.0, as indicated in the enlarged plots (see the insert in Figure 9(b)). Table 2 lists the unassigned weak peaks.

3.4.3 ^{1}H spectra

^{1}H MAS NMR spectra in Figure 9(c) shows two strong ^{1}H peaks for each phase: at 0.03 and 5.68 ppm for HAp: S1 and at 5.56 and 10.56 for DCPD: S2. According to the literature, the 0.0 ppm peak of S1 is distinctly located in the OH group at an A-site of the HAp lattice, sometimes designated as a structural OH [22]. A large, strong, and broad peak at 5.6 ppm is attributed to H_2O molecules adsorbed on HAp crystals because Jarlbring et al. [25] could not find any correlation between the lattice PO_4 and proton of 5.6 $\delta(^{1}H)$ from their ^{1}H–^{31}P CP-MAS HETCOR (heteronuclear correlation) experiment along the ^{1}H dimension ^{1}H–$\{^{31}P\}$. The same assignment was found in the preceding studies [21,28,29]. Note that the peak intensity of this adsorbed H_2O is larger than that of the lattice OH at 0.0 ppm, in accordance with Sfihi and Rey [23] and Jarlbring et al. [25]. The latter group [25] detected both peaks with a comparable intensity, despite heat treating their sample at 105°C for 24 h. This implies

Table 1: The NMR samples, pH of soaking solution (1 M K_2HPO_4), soaking time (d), and signal-acquiring modes; soaking temperature: 37°C

Phase: sample	pH	Period (days)	Nuclei, NMR mode
HAp:S1	7	1	^{1}H, MAS; ^{31}P: MAS & $^{1}H \rightarrow {}^{31}P$ CP-MAS
DCPD:S2	6	1	^{1}H, MAS; ^{31}P: MAS & $^{1}H \rightarrow {}^{31}P$ CP-MAS
HAp:S3	10	2	^{13}C: $^{1}H \rightarrow {}^{13}C$ CP-MAS

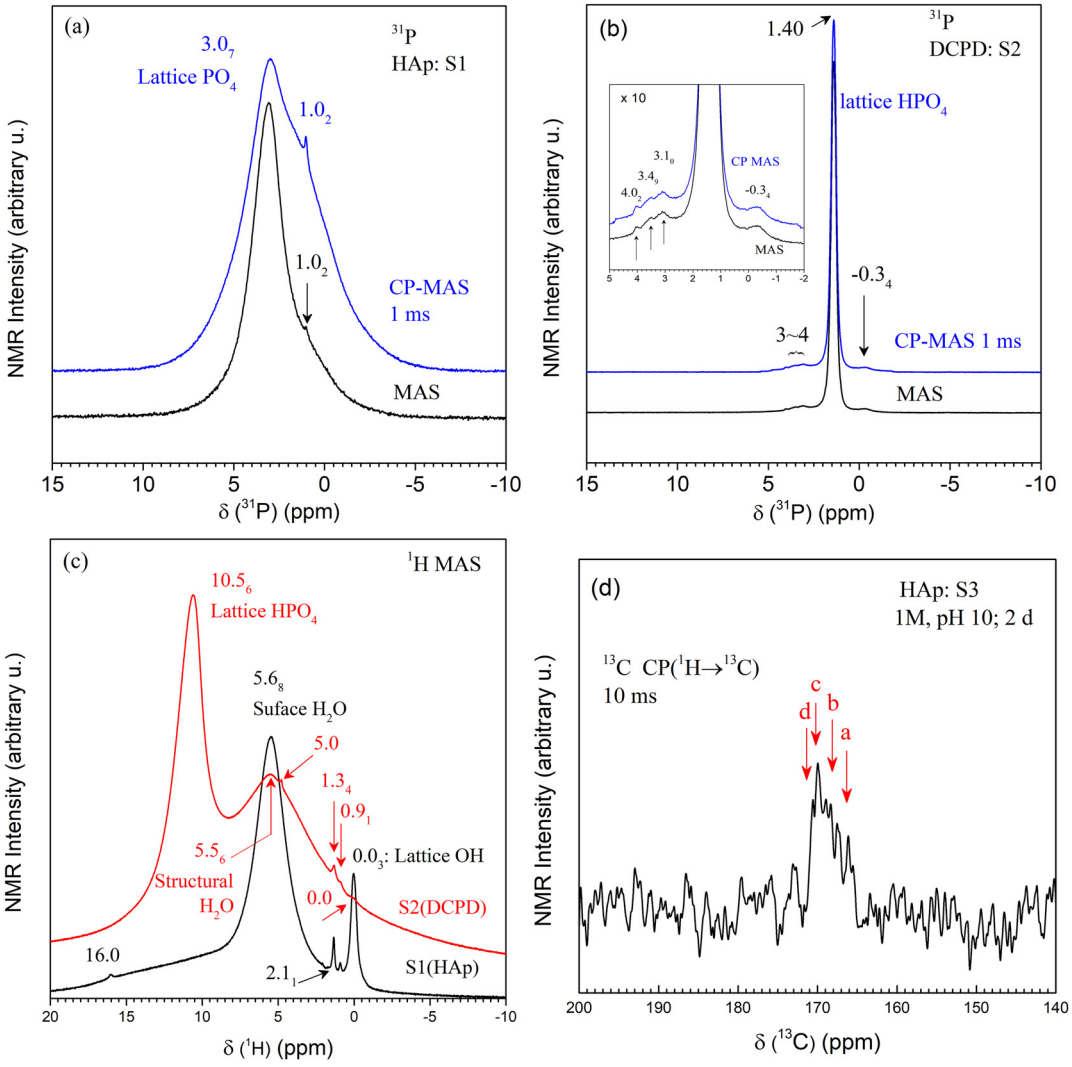

Figure 9: MAS and CP-MAS NMR spectra for HAp: S1 and DCPD: S2. (a) and (b) ^{31}P MAS and CP-MAS NMR spectra; (c): ^{1}H MAS NMR spectra. See text and Table 1 for sample derivation. Assignments were given to major peaks. (d) ^{13}C CP-MAS spectrum of HAp: S3 from CC in 1 M K_2HPO_4, pH 10, for 2 days. Arrows a–d indicate peak positions found for ^{13}C-enriched apatite [23,32].

that H_2O molecules are quite tightly bound to crystallite surfaces. In this study, samples were dried at 60°C for 12 h. Such a moderate drying condition is favored for a relatively large amount of H_2O remaining on HAp surfaces. Later in Section 4.2.2 a possible role of such intercrystallite H_2O is discussed.

Because a larger chemical shift δ(^{1}H) is associated with a higher acidity of proton, a prominent ^{1}H peak at 10.56 ppm of DCPD:S2 in Figure 9(c) should be assigned to the proton of the lattice HPO_4 group, rather than to H_2O molecules adsorbed on the surface or involved in the structure of DCPD. This peak assignment is consistent with the reported peaks of 10.4 ppm [22,31] and 10.2 ppm [32,34]. Yesinowski and Eckart [22] designated their 10.4 ppm peak as the signal of an acidic proton. Hence, a broad ^{1}H peak centered at 5.58 ppm of DCPD:S2 is attributable to the structural water. Pourpoint et al. [34] observed a doublet ^{1}H peak at 4.8 and 6.6 ppm using a high-spinning rate (33 kHz). According to their first-principle calculation, the 5 ppm ^{1}H peak should be an envelope of four peaks, corresponding to four different lattice sites in DCPD. In contrast, Yesinowski and Eckart assigned a 6.4 ppm ^{1}H peak to structural H_2O of DCPD [22].

Both HAp and DCPD showed a few minor signals in the range of 0.9–2.1 ppm of δ(^{1}H) in Figure 9(c), while Jäger et al. [24] reported very distinct and narrow line signals in the same δ(^{1}H) range for their nano-sized apatite. Osman et al. interpreted those groups as originated from OH groups with different alignments

Table 2: NMR chemical shifts δ(^{1}H) and δ(^{31}P) for samples of the present study [*][1)]; HAp: S1 and DCPD: S2. Several data were taken from selected references [22,25,29–32,34]. (§)

Locations	δ (^{1}H) (ppm)	δ (^{31}P) (ppm)	Comments & Ref.
Apatite lattice	OH^-	PO_4^{3-}	
	0.0_3 (S1) m,s[a]	3.0_7 (S1) vs,s	[*][b]
	0.2 vs,s	—[c]	[22]
	0.1 vs,s	—	[29]
	—	2.9	F-apatite [25]
	0 s,s	3.0 s,s	2-D [32]
	1.1 (0.8 + 1.3) vw	—	[29]
DCPD lattice	HO-PO_3	HPO_4	
	10.5_6 (S2) vs,s	1.40 (S2) vs,s	[*]
	10.2 vw	1.7	[32]
	10.2 Vs,s	1.6	[34]
	10.4 vs,s	—	[31]
	12.1 as a shoulder	3.05	2-D[d] [30]
DCPD lattice H_2O	H_2O		
(structural)	5.5_6 (S2) vs,b	—	[*]
	4.1 + 6.5[e] m,b	—	[34]
Surface	H_2O adsorbed	H_xPO_4	
(physi-/chemisorbed) [f]	—	0.8 sh	HPO_4 F-apatite[g] [25]
	—	5.4 sh	PO_4^{3-} F-apatite [25]
	5.6_8 (S1) vs	—	[*] HAp
	5.5 s,s	—	HAp [22]
	5.5 m,b (4.5 + 6.6)	—	DCPD [31]
	5.8	—	HCA: 2-D [30]
	5.4	—	HAp + TCP; 2-D [32]
	5.1	—	[29]
Unassigned	–	1.0_3 (S1) w,s	[*]
	–	-0.3_4, 3.1_0, 3.4_9, 4.0_2 (S2)	[*]
	0.0 vw (S2)	—	[*]
	0.9_1~0.9_3 w,s (S1, S2)	—	[*] [29]
	1.3_4 m,s (S1, S2)	—	[*] [29]
	2.1_1 vw,sh (S1)	—	[*] [29]
	$16._0$ vw,s (S2)	—	[*]
Other phase			
DCPA (monetite)	16_2 vw	—	HPO_4 [22]
	13.2, 15.8 vs,s		HPO_4 [31]

[a] vs, s, m, and w are abbreviations for very strong, strong, medium, and weak, respectively. The symbols s, b, and sh following "," represent strong, broad, and shoulder. And the symbols (m,s), (vs,s), or (w,s) denote a medium and sharp peak, a very strong and sharp peak, and a weak and sharp peak; sh stands for a shoulder of a dominant peak. Notation was added to the selected peaks. [b] *: Present study. S1 (HAp): 1 M K_2HPO_4, pH 7, 1 d; S2 (DCPD): 1 M K_2HPO_4: pH 6, 1 d. [c] Symbol – (dash) means no data available or given. [d] 2-D indicate the peak was given on a slice spectrum of the 2-D projection. [e] Symbol + means that peaks appeared as a doublet or were deconvolutable to component peaks. [f] Physically or chemically adsorbed on surfaces of crystals. [g] F-apatite: fluorapatite ($Ca_5(PO_4)_3F$).

along the c axis of HAp [29]. Table 2 followed their assignment. Figure 9(c) has another minor δ(^{1}H) peak at 16.0 ppm. Yesinowski and Eckert assigned the signal to HPO_4 of DCPA [22]. Although the chemical shift of 16 ppm corresponds to a highly acidic proton, probably this assignment would not be adequate. Yu et al. gave a pair of sharp ^{1}H peaks for DCPA at 13.2 and 15.8 ppm. Therefore, ^{1}H: 16 ppm peak observed in the present study was presented unassigned in Table 2.

3.4.4 ^{13}C NMR spectra

Figure 9(d) demonstrates a ^{1}H → ^{13}C CP-MAS NMR spectrum of the sample HAp:S3. Despite the relatively low signal to noise ratio, Figure 9(d) clearly exhibits a peak, extending from 150 to 172 ppm. A hump around 173 ppm may be a noise. Babonneau et al. have already reported the presence of a ^{13}C peak for ^{13}C-enriched HCA, and the peak showed four local maxima [26]. This

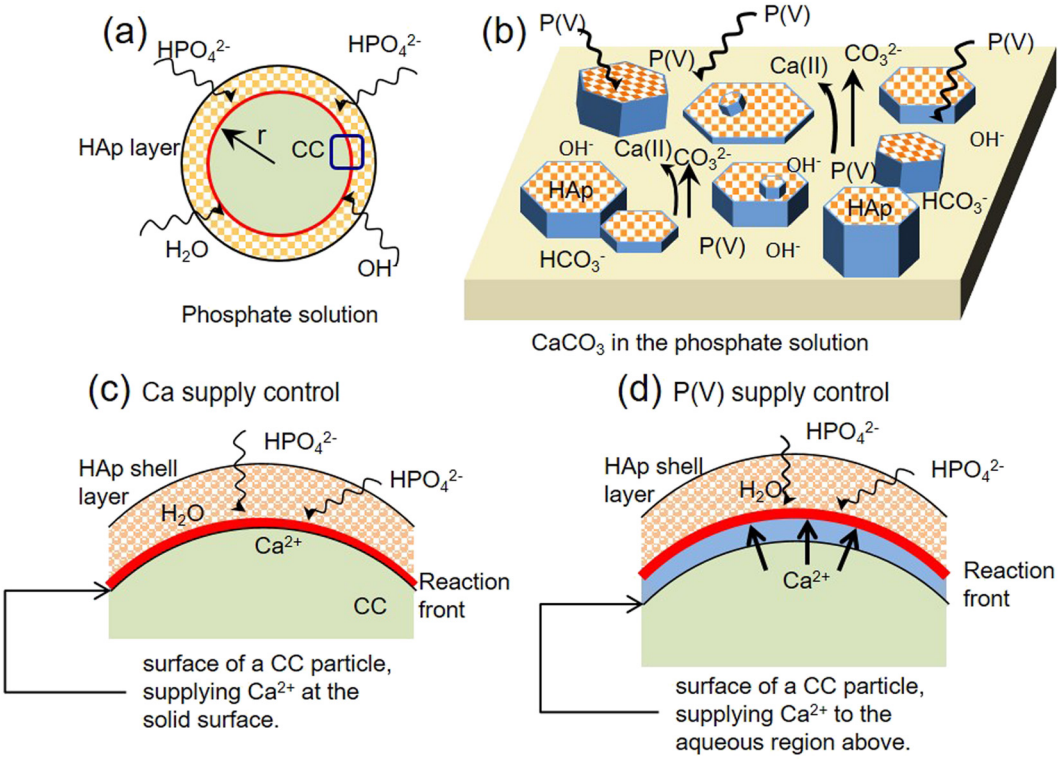

Figure 10: (a) A reaction model of a CC core with a HAp layer, allowing migration of species such as HPO_4^{2-} ions to the reaction front. A square part is enlarged in (c) and (d). (b) An enlarged schematic model of the reaction front at stage I. The surface was in contact with phosphate solution. Hydroxy, calcium, and phosphate ions are presented as OH, Ca(II), and P(V). (c) and (d): Structures near the reaction front in stages I_{tr} and II (see text).

suggested that the presence of at least four different carbonate sites. Sfihi and Rey reported ^{13}C peaks of CO_3^{2-} at 168.5 and 170 ppm for their fluorapatite but found no peak at 166 ppm [23]. Moreover, they stated in their paper that "the CO_3 groups at 168.5 ppm will not be located in the bulk but near the surface." If they meant the presence of the 168.5 ppm CO_3^{2-} so near the surface that they would "talk" (exchange the nuclear magnetic moments) with component species on the surface like adsorbed H_2O, correlation should be detected between the carbonate ions and surface water molecules. Unfortunately, however, Babonneau et al. did not find such a correlation between CO_3^{2-} and H_2O via ^1H–^{13}C CP-MAS NMR HETCOR experiments [26]. But the carbonate ions detected here are surely in the lattice sites. Leroy et al. employed a high-end NMR technology, dynamic nuclear polarization, and carried out a full analysis of the carbonate ion sites, regardless of whether the CO_3^{2-} ions occupy the OH (A) sites or PO_4 (B) sites of the apatite lattice [35]. They considered the substitution pairs of A and B sites, and lattice structure, before finalizing the assignments. In brief, the whole peak involved five component contributions, showing A/B substitution ($OH^- + PO_4^{3-} \rightarrow 2CO_3^{2-}$) gave $\delta(^{13}C)$ of 166.5 and 168.0 ppm, while B/B one ($Ca^{2+} + 2PO_4^{3-} \rightarrow Ca^{2+}$ vacancy $+ 2CO_3^{2-}$) resulted in the peaks at 168.3, 170.1, and 171.0 ppm. In this study, the ^{13}C signals were located within the range of those ^{13}C signal assignments [26,35]. Thus, it is reasonable to conclude that CO_3^{2-} ions were involved in the A and B lattice sites of the HAp sample. The conversion from CC and the precipitation pH conditions might favor a carbonate ion involvement.

4 Discussion

4.1 Conversion reaction analysis

4.1.1 The rate analysis of conversion reactions in the earliest period

SEM images in Figures 3 and 5 indicate that soaked particles should have a core (CC)–shell (HAp) structure.

Sharp decrease in $I(t)/I_0$ as can be observed in Figure 8 for the (104) diffraction of CC, which implies that most of conversion reaction finishes within 3 h (in stage I). Such a fast reaction must be accompanied by a fast transportation of reactants to the reaction front. Based on these observations, a reaction model is proposed as presented in Figure 10, with following assumptions:

(a) Spherical CC particles in contact with K_2HPO_4 solution, as shown in Figure 10(a).
(b) Active site density remains constant on the reaction front.
(c) Component species can freely migrate to the reaction front.

Figure 10(b) illustrates the formation process of the HAp shell layer. For a simple illustration, hexagonal pieces are aligned flat, as drawn here, with their (002) plane on CC surface. But in reality, CC is polycrystalline and should expose a variety of lattice planes to solution, even if epitaxy would be applicable between calcite and HAp. A random assembly of crystallites is also supported by the observation [36] that wet chemically derived HAp crystallites exhibit a few lattice images randomly stacked when observed under a transmission electron microscope.

A primitive analysis of the reaction rate is only valid in stage I ($t < 3$ h) because as shown in Figure 8, the conversion precedes in some different modes in later stages, I_{tr} and II. Minh et al. employed arbitrarily two different diffusion models, depending on the reaction temperature in their systems of CC conversion to HAp [3]. Our model assumes a diffusion as described in (c) above. The assumption (b) is the key for the present analysis. It means that the rate of decrease in volume V of a CC particle during conversion is proportional to the surface area S. This leads to equation (2) with k' as the rate constant

$$-\mathrm{d}V/\mathrm{d}t = k'S \tag{2}$$

Substituting the particle radius r to V and S and applying $V \propto I(t)/I_0$, equation (2) can be modified to equation (3):

$$(I(t)/I_0)^{1/3} = -kt + C \tag{3}$$

Here C is the constant of integral and k is the apparent rate constant related to the XRD intensity ratio in CC → HAp conversion. Note again this equation (2) is only valid at the beginning stage of the conversion. From linear correlations between $(I(t)/I_0)^{1/3}$ and the soaking period t in Figure 11(a) (0.1 M, pH 10) and (b) (1 M, pH 10), the apparent conversion rate constant k is derived for each temperature and listed in the inserted tables. Figure 11(c) demonstrates an Arrhenius-type correlation between k $(1/h)$ and $1/T$ $(1/K)$,

$$k = f \exp(-\Delta\varepsilon/\mathrm{RT}) \tag{4}$$

Here f is the frequency factor and $\Delta\varepsilon$ is the apparent activation energy. Thus, the derived $\Delta\varepsilon$ for both 0.1 M and 1 M K_2HPO_4 solutions is practically identical and close to $\Delta\varepsilon$ (4.3 kcal/mol = 35.7 kJ/mol) for $H_2PO_4^-$ ion diffusion in NaH_2PO_4 aqueous solution (∞ dilution), as given by Krauss and Sinks [37]. This observation, therefore, implies that the diffusion of phosphate ions controls the conversion reaction. In other words, Ca^{2+} and OH^- would be sufficiently available at the reaction sites to wait for phosphate ions. The frequency factor of 1 M solution (the upper line in Figure 11(c)) is an order of magnitude greater than that for 0.1 M solution. This can be simply interpreted as the effect of the phosphate ion concentration.

4.1.2 Primary crystallite size and ripening

Application of Scherrer formula, equation (5), to broadened XRD lines derives an approximate size (τ) of a primary crystal in a polycrystalline phase [19].

$$\tau = K\lambda/(\mathrm{FWHM} \cdot \cos\,\theta) \tag{5}$$

Here K is the Scheler constant ($K = 0.9$), λ is the X-ray wavelength (Cu Kα; 0.1540 nm), full width at half maximum (FWHM) is the line width, and θ is the diffraction angle. The XRD profiles of HAp in Figures 2, 4, and 6 are accompanied by the sharp (104) line of calcite (CC), and this peak is used to calibrate XRD machine broadening before the derivation of τ for samples. Figure 12 plots the so-calculated HAp crystallite size τ as a function of soaking period t (h). τ increases quickly to ~30 nm within 12 h. This reaction range corresponds to stages I and I_{tr} in Figure 8. Unfortunately, It was impossible to derive τ for sample after being soaked for $t < 7$ h because the (002) diffraction is too weak. Then τ increases slowly and reaches ~40 nm at 240 h (10 days; stage II). The size is in accord with that of HAp nanoparticles derived wet chemically [36]. Results in Figure 12 imply that seven or eight pieces of primary crystallites are assembled to form a petal-like HAp crystallite layer with a size of approximately 250 nm, as shown in Figure 5.

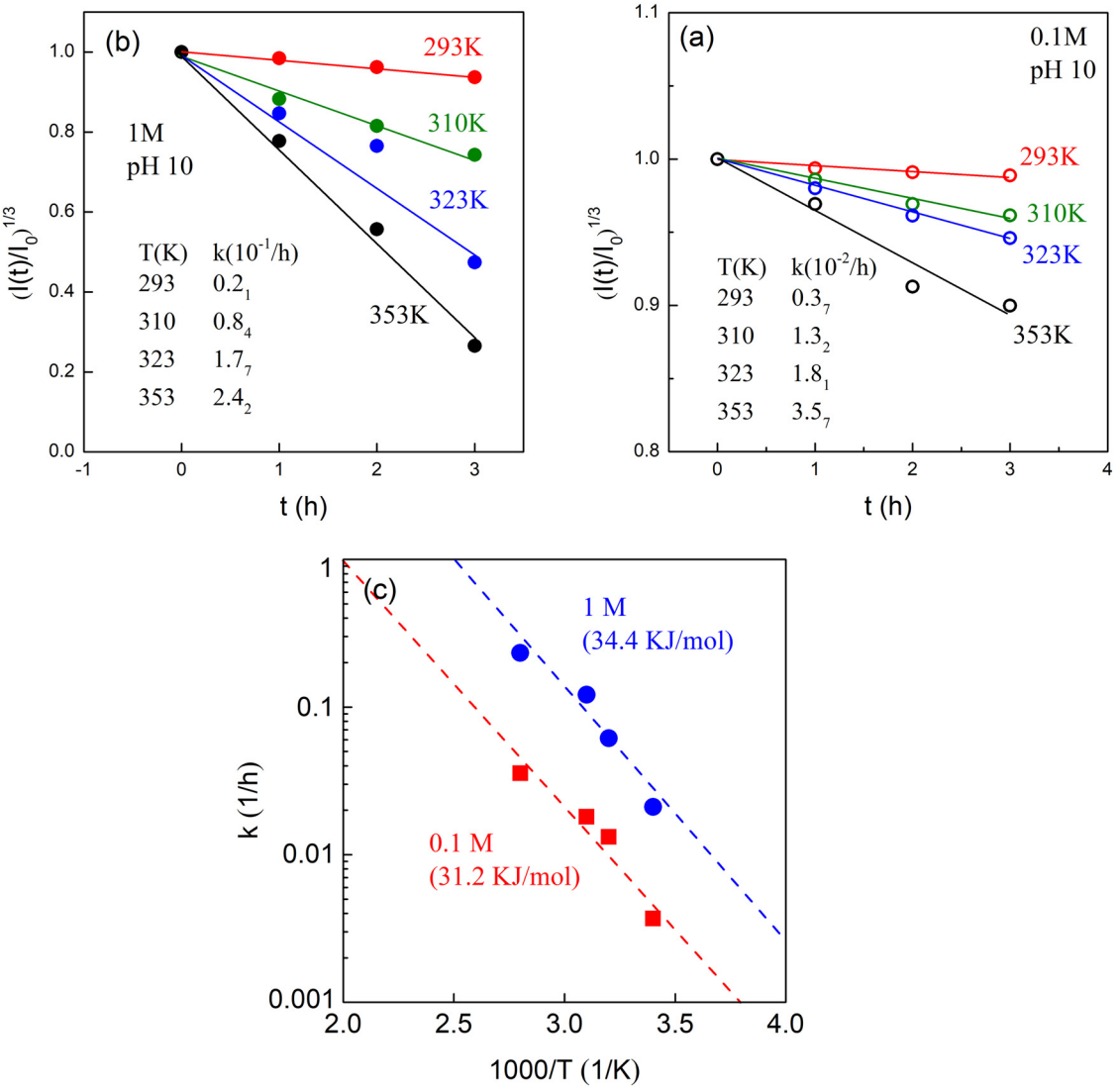

Figure 11: Plots of $(I(t)/I_0)^{1/3}$ vs soaking period t (h) for CC → HAp conversion reaction at 293–353 K (20°C–80°C) in (a) 0.1 M K_2HPO_4 and (b) 1 M K_2HPO_4. The inserted tables list the apparent rate constant k derived from equation (2). (c) The broken lines represent Arrhenius-type correlations (Equation (3)), and the derived values of the apparent activation energy are in the parentheses.

4.1.3 Growth of a petal-like crystal

The changes in the size of primary crystal in Figure 12 indicate that the mechanism of HAp formation is different in stages I and II. A drastic growth of primary crystals in stage I (t < 3 h) is achieved only under sufficient supply of Ca^{2+}, HPO_4^{2-}, and OH^- ions to the reaction front, as described in Figure 10(b). In the course of conversion, the primary crystallites are formed in random orientations with respect to the CC surfaces. They grow into contact and fuse with each other, leaving some space among primary crystallite assemblies. The presence of H_2O in these spaces is supported by the large ^1H NMR band assigned to surface H_2O (5.6 ppm in $\delta(^1H)$: Figure 9(c)). The fused crystallites are assembled repeatedly, which grow into a floret-like agglomerations in stages I_{tr} and II. Along such crystallizing events, the CC particles would continue to be dissolved. Their volumes will decrease or keep shrinking. Therefore, Ca^{2+} ions are always supplied sufficiently at the reaction front, and phosphate ions should migrate into primary crystallites via water channels. Both ions take OH– from solution and form agglomerated secondary crystals. This is a plausible growth model. It considers the apparent activation energy ($\Delta\varepsilon$; Figure 11(c)) of CC → HAp conversion, which is in a good agreement with that of H_2PO_4 diffusion [37].

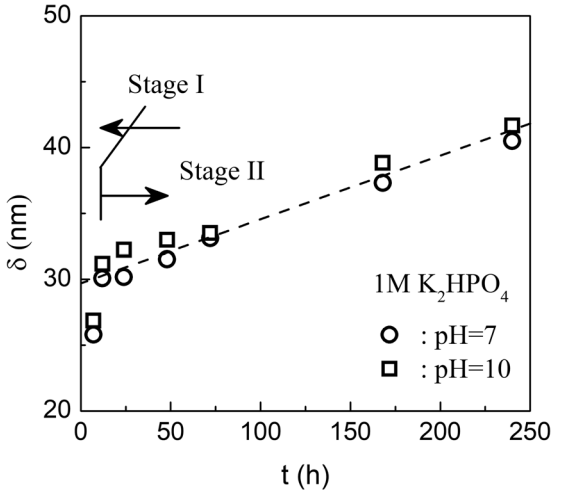

Figure 12: Crystallite size τ (nm) of HAp precipitated in 1 M K_2HPO_4 solutions of pH 7 (○) and pH 10 (□) derived from Scherrer equation, i.e., Equation (8) [19]. Conversion stages I and II are indicated as in Figure 8(a). The broken line is a guide for eyes.

4.2 Microstructure of HAp agglomerates

4.2.1 Formation of hollow HAp particles

Calcite is sparingly soluble in water, with a solubility product K_{sp} being 3.36×10^{-9} (mol/L)^2 [38]. The solubility of 58 μM/L (~0.58 mg/100 g-H_2O) is high enough to supply component ions to the aqueous medium in contact, according to equation (6a).

$$CaCO_3 \rightarrow Ca^{2+} + CO_3^{2-} \text{ [dissolution]} \quad (6a)$$

Extremely low-solubility product of HAp (~5×10^{-118}) [39] and the stability of HAp [7] are thermodynamically favorable for HAp precipitation when its components are available. At the very beginning (stage I), the liberated Ca^{2+} ions found many phosphate ions on particle surfaces (Figure 10(b)), and hence they instantly form a HAp layer. In later stages I_{tr} and II, the phosphate ions migrate through the layer, driven by the concentration gradient that is established around particles, to the reaction front. Another possible way of deposition of a Ca-P phase is a direct reaction due to the withdrawal of Ca^{2+} ions from solid CC by HPO_4^{2-} ions, arriving at the surface (equation (6b)).

$$CaCO_3 \xrightarrow{HPO_4^{2-}} Ca^{2+} \text{ (Ca – P) [surface reaction]} \quad (6b)$$

This case implies that the rate of free Ca^{2+} ion supply is too small to meet the frequency of HPO_4^{2-} and OH^- ions to arrive at particular reaction sites. That is, the apparent activation energy should be associated with CC dissociation but not with phosphate ion diffusion. This is similar to the direct conversion of OCP to HAp reported by Tseng et al. [40]. If equation (6b) were valid, the precipitation should always take place on CC surface, as depicted in Figure 10(c), until the CC is exhausted. This would lead to solid particles [41,42].

In contrast, equation (6a) implicitly represents that calcium ions should be liberated into aqueous region, adjacent to CC surface, as presented in Figure 10(d). They wait for phosphate ions to reach the inner surface of the HAp shell or the reaction front. That is, the conversion reaction allows the HAp layer to be separated from the surface in later stages. This is a plausible interpretation for formation of hollow HAp particles detected in Figures 3 and 7. The OH ions will be supplied via water dissociation equilibrium when they are consumed at the reaction front. Such a scheme is compatible with the apparent activation energy of the net conversion reaction and apparent activation energy of H_2PO_4 ion diffusion in aqueous solution [37,43–45]. In both cases in Figure 10(c and d), HAp grows inwardly as in the case of HAp nano-rod array grown on sodium calcium silicate glass substrate which were soaked in 0.01 M Na_2HPO_4 solution [46–49].

4.2.2 Net conversion reaction

Equation (7) is a probable net reaction for CC → HAp conversion when a high pH (>10) stabilizes CO_3^{2-} (pK_2 (H_2CO_3) = 10.33 [8,38]):

$$5CaCO_3 + 3HPO_4^{2-} + 4OH^- \rightarrow Ca_5(PO_4)_3(OH) + 5CO_3^{2-} + 3H_2O \quad (7)$$

In a lower pH region, where an insufficient amount of OH^- is available, OH^- will be supplied via $H_2O \rightarrow H^+ + OH^-$. Then equation (7′) is derived.

$$5CaCO_3 + 3HPO_4^{2-} + H_2O \rightarrow Ca_5(PO_4)_3(OH) + 5CO_3^{2-} + 4H^+ \quad (7')$$

The yielded H^+ would be scavenged by carbonate ions to form HCO_3^-, (pK_1 (H_2CO_3) = 6.33) [8,38]. Then equation (8) replaces equation (7) to represent the net reaction that may occur when pH < 10:

$$5CaCO_3 + 3HPO_4^{2-} + H_2O \rightarrow Ca_5(PO_4)_3(OH) + 5HCO_3^- + OH^- \quad (8)$$

Equation (8) explains why the pH of K_2HPO_4 solutions increased after the completion of the reaction with initial pH of solutions being adjusted to 7 or 10. With the solubility 6.15×10^{-4} mol of CO_2 (100 kPa) in 1 mol water

and volume fraction of CO_2 in air (408 ppm) [38], the solubility limit of CO_2 in 20 mL solution is as low as ~2.8 nano mol, and the expected CO_2 evolution from 0.5 g CC was 5 m mol. In consequence, H^+ in equation (7′) should drive the CO_2–H_2O equilibria to favor the formation of CO_2. This explains the bubbling observed in the course of reaction in solution of pH 7. Equation (9) then represents the CC → HAp conversion accompanying CO_2 evolution:

$$5CaCO_3 + 3HPO_4^{2-} + 2H_2O \rightarrow Ca_5(PO_4)_3(OH) + 5CO_2 + 6OH^- \quad (9)$$

5 Conclusion

Based on the results obtained in this study, following conclusions can be drawn:

(1) Soaking CC for 72 h in 1 M K_2HPO_4 solution, only DCPD is yielded with pH ≤ 6 while only HAp was obtained with pH ≥ 7. DCPD shows a morphology consisting of assemblies of long rectangular crystallites extending outward. The morphology of HAp consists of hollow shells with petal-like crystallites forming porous shell walls. Such a porous shell structure is more conducive to tissue growth.

(2) By analyzing CC to HAp conversion rate at a beginning stage, an apparent activation energy of about 34 kJ/mol has been obtained, which is in accordance with the diffusion of $H_2PO_4^-$ in aqueous solutions.

(3) Primary crystal size of HAp, derived due to Scherrer equation, shows a rapid growth within the first 7 h and a slow ripening afterward.

(4) Results of MAS and CP-MAS NMR spectra can be summarized as below: (a) prominent peaks of ^{31}P indicate HPO_4^{2-} and PO_4^{3-} in the lattice sites of DCPD, and PO_4^{3-} in the lattice sites of HAp. (b) ^1H peaks of HAp implies that H_2O and OH are adsorbed on its crystallite surfaces. (c) HAp shows a tiny ^{13}C peak, indicating the presence of CO_3^{2-} in both A (OH) and B (PO_4) sites of the HAp lattice.

Acknowledgments: This work was supported by the Chinese 02 Special Fund (Grand No. 2017ZX02408003), the Innovative Research Team Program of Henan University of Science and Technology (Grant No. 2015XTD006), and the Natural Science Fund Cultivation Project of Henan Province (Grant No. 162300410087).

Conflict of interest: The authors declare no conflict of interest regarding the publication of this paper.

References

[1] Xia X, Chen J, Shen J, Huang D, Duan P, Zou G. Synthesis of hollow structural hydroxyapatite with different morphologies using calcium carbonate as hard template. Adv Powder Technol. 2018;29(7):1562–70.

[2] Ruffini A, Sprio S, Tampieri A. Study of the hydrothermal transformation of wood-derived calcium carbonate into 3D hierarchically organized hydroxyapatite. Chem Eng J. 2013;217:150–8.

[3] Minh DP, Rio S, Sharrock P, Sebei H, Lyczko N, Tran ND, et al. Hydroxyapatite starting from calcium carbonate and orthophosphoric acid: synthesis, characterization, and applications. J Mat Sci. 2014;49(12):4261–9.

[4] Engin A, Girgin I. Synthesis of hydroxyapatite by using calcium carbonate and phosphoric acid in various water–ethanol solvent systems. Cent Eur J Chem. 2009;7(4):745–51.

[5] Verwilghen C, Chkir M, Rio S, Nzihou A, Sharrock P, Depelsenaire G. Convenient conversion of calcium carbonate to hydroxyapatite at ambient pressure. Mat Sci Eng C. 2008;29(3):771–3.

[6] Portela da Silva NM, Espitalier F, Nzihou A. Precipitation process of calcium phosphate from calcium carbonate suspension. KONA Powder Part J. 2016;33:219–27.

[7] Pourbaix M. Atlas of Electrochemical Equilibria in Aqueous Solutions. Oxford: Pergamon Press; 1966. Chap. IV, §18.2, p. 504–515. Pourbaix M (1966), Atlas of electrochemical equilibria in aqueous solutions, 1st edn., Chap. IV, §18.2. Pergamon Press, Oxford, England.

[8] Chow LC. Next generation calcium phosphate-based biomaterials. Dental Mater J. 2009;28(1):1–10.

[9] Sethmann I, Luft C, Kleebe H-J. Development of phosphatized calcium carbonate biominerals as bioactive bone graft substitute materials, Part I: incorporation of magnesium and strontium ions. J Funct Biomater. 2018;9:69.

[10] Fujita Y, Yamamuro T, Nakamura T, Kotani S, Ohtsuki C, Kokubo T. The bonding behavior of calcite to bone. J Biomed Mater Res. 1991;25(8):991–1003.

[11] Neo M, Kotani S, Fujita Y, Nakamura T, Yamamuro T, Bando Y, et al. Differences in ceramic-bone interface between surface-active ceramics and resorbable ceramics: a study by scanning and transmission electron microscopy. J Biomed Mater Res. 1992;26(2):255–67.

[12] Ban I, Stergar J, Maver U. NiCu magnetic nanoparticles: review of synthesis methods, surface functionalization approaches, and biomedical applications. Nanotechnol Rev. 2018;7(2):187–207.

[13] Zang ST, Chang SJ, Shahzad MB, Sun X, Jiang X, Yang H. Ceramics-based drug delivery system: a review and outlook. Rev Adv Mater Sci. 2019;58(1):82–97.

[14] Guo SH, Fu DW, Utupova A, Sun D, Zhou M, Jin Z, et al. Applications of polymer-based nanoparticles in vaccine field. Nanotechnol Rev. 2019;8(1):143–55.

[15] Kokubo T, Yamaguchi S. Simulated body fluid and the novel bioactive materials derived from it. J Biomed Mater Res Part A. 2019;107(5):968–77.
[16] Manohar CS, Kumar BS, Sadhu SPP, Srimadh SK, Muthukumar VS, Venketesh S,et al. Novel Lead-free biocompatible piezoelectric hydroxyapatite (HA) – BCZT (Ba0.85Ca0.15Zr0.1Ti0.9O3) nanocrystal composites for bone regeneration. Nanotechnol Rev. 2019;8(1):61–78.
[17] Ohtsuki C, Kokubo T, Neo M, Kotani S, Yamamuro T, Nakamura T, et al. Bone-bonding mechanism of sintered β-3CaO.P_2O_5. Phosphorus Res Bull. 1991;1:191–6.
[18] Fu H, Rahaman MN, Day DE. Effect of process variables on the microstructure of hollow hydroxyapatite microspheres prepared by a glass conversion method. J Am Ceram Soc. 2010;93(10):3116–23.
[19] Cullity BD. Elements of X-ray diffraction, 2nd edn. MA: Addison-Wesley, Reading; 1978; chap. 3–7 and 14–11.
[20] Kallaste T, Memliher J. Apatite varieties in extant and fossil vertebrate mineralized tissues. J Appl Crsyt. 2005;38(4):587–94.
[21] Schröder R, Pohlit H, Schüler T, Panthöfer M, Unger RE, Frey H, et al. Transformation of vaterite nanoparticles to hydroxycarbonate apatite in a hydrogel scaffold: relevance to bone formation. J Mater Chem B. 2015;3(35):7079–89.
[22] Yesinowski JP, Eckert H. Hydrogen environments in calcium phosphates: ^{1}H MAS NMR at high spinning speeds. J Am Chem Soc. 1987;109:6274–82.
[23] Sfihi H, Rey C. 1-D and 2-D double heteronuclear magnetic resonance study of the local structure of type b carbonate fluoroapatite, magnetic resonance in colloid and interface science. Nato ASI Ser II. 2002;76:409–22.
[24] Jäger C, Welze T, Meyer-Zaika W, Epple M. A solid-state NMR investigation of the structure of nanocrystalline hydroxyapatite. Magn Reson Chem. 2006;44:573–80.
[25] Jarlbring M, Sandström DE, Antzutkin ON, Forsling W. Characterization of active phosphorus surface sites at synthetic carbonate-free fluorapatite using MAS NMR single-pulse 1H, 31P, and 31P CP. Langmuir. 2006;22(10):4787–92.
[26] Babonneau F, Bonhomme C, Hayakawa S, Osaka A. Solid state NMR characterization of nano-crystalline hydroxy-carbonate apatite using 1H-31P-13C triple resonance experiments. Mater Res Soc Symp Proc. 2007;984:6.
[27] Barheine S, Hayakawa S, Jäger C, Shirosaki Y, Osaka A. Effects of disordered structure of boron-containing calcium phosphates on their *in vitro* biodegradability. J Am Ceram Soc. 2011;94(8):2656–62.
[28] Davies E, Duer MJ, Ashbrook SE, Griffin JM. Applications of NMR crystallography to problems in biomineralization: refinement of the crystal structure and ^{31}P solid-state NMR spectral assignment of octacalcium phosphate. J Am Chem Soc. 2012;134(30):12508–15.
[29] Osman MB, Diallo-Garcia S, Herledan V, Brouri D, Yoshioka T, Kubo J, et al. Discrimination of surface and bulk structure of crystalline hydroxyapatite nanoparticles by NMR. J Phys Chem C. 2015;119:23008–20.
[30] Mathew R, Turdean-Ionescu C, Yu Y, Stevensson B, Izquierdo-Barba I, García A, et al. Proton environments in biomimetic calcium phosphates formed from mesoporous bioactive CaO–SiO_2–P_2O_5 Glasses *in vitro*: insights from solid-state NMR. J Phys Chem C. 2017;121(24):13223–38.
[31] Yu Y, Guo H, Pujari-Palmer M, Stevensson B, Grins J, Engqvist H, et al. Advanced solid-state ^{1}H/^{31}P NMR characterization of pyrophosphate-doped calcium phosphate cements for biomedical applications: the structural role of pyrophosphate. Ceram Int. 2019;45:20642–55.
[32] Konishi T, Yamashita K, Nagata K, Lim PN, Thian ES, Aizawa M. Solid-state nuclear magnetic resonance study of setting mechanism of β-tricalcium phosphate-inositol phosphate composite cements. J Phys Mater. 2019;2:034007.
[33] Tseng Y-H, Mou Y, Chen P-H, Tsai TWT, Hsieh C-I, Mou C-Y, et al. Solid-state P-31 NMR study of the formation of hydroxyapatite in the presence of glutaric acid. Magn Reson Chem. 2008;46(4):330–4.
[34] Pourpoint F, Gervais C, Bonhomme-Coury L, Azaîs T, Coelho C, Mauri F, et al. Calcium phosphates and hydroxyapatite: solid-state NMR experiments and first-principles calculations. Appl Mag Reson. 2007;32(4):435–57.
[35] Leroy C, Aussenac F, Bonhomme-Coury L, Osaka A, Hayakawa S, Babonneau F, et al. Hydroxyapatites: key structural questions and answers from dynamic nuclear polarization. Anal Chem. 2017;89(19):10201–7.
[36] Hayakawa S, Kanaya T, Tsuru K, Shirosaki Y, Osaka A, Fujii E, et al. Heterogeneous structure and *in vitro* degradation behavior of wet-chemically derived nanocrystalline silicon-containing hydroxyapatite particles. Acta Biomater. 2013;9(1):4856–67.
[37] Krauss CJ, Spinkes JWT. Temperature coefficients for self-diffusion in solution. 1954;32(2):71–78.
[38] Rumble JR, editor. CRC handbook of chemistry and physics, 100th edn. NM, USA: CRC Press; 2019.
[39] Tsuru K, Kubo M, Hayakawa S, Ohtsuki C, Osaka A. Kinetics of apatite deposition of silica gel dependent on the inorganic ion composition of simulated body fluids. J Ceram Soc Jpn. 2001;109(1269):412–8.
[40] Tseng Y-H, Mou C-Y, Chan JCC. Solid-state NMR study of the transformation of octacalcium phosphate to hydroxyapatite: a mechanistic model for central dark line formation. J Am Chem Soc. 2006;128(21):6909–18.
[41] Zhang Y, Chai Z, Volinsky AA, Tian B, Sun H, Liu P, et al. Processing maps for the Cu-Cr-Zr-Y alloy hot deformation behavior. Mater Sci Eng A. 2016;662(4):320–9.
[42] Lin NM, Xie RZ, Zou JJ, Li D, Yuan S, Wang Z, et al. Surface damage mitigation of titanium and its alloys *via* thermal oxidation: a brief review. Rev Adv Mater Sci. 2019;58(1):132–46.
[43] Long F, Guo X, Song K, Jia S, Yakubov V, Li S, et al. Enhanced arc erosion resistance of TiB_2/Cu composites reinforced with the carbon nanotube network structure. Mater Des. 2019;183:108136.
[44] Nakonieczny DS, Basiaga M, Sambok A, Antonowicz M, Paszenda Z, Ziębowicz AM, et al. Ageing of zirconia dedicated to dental prostheses for bruxers part 1: influence of accelerating ageing for surface topography and mechanical properties. Rev Adv Mater Sci. 2019;58(1):189–94.
[45] Hu C, Sun JX, Long C, Wu L, Zhou C, Zhang X. Synthesis of nano zirconium oxide and its application in dentistry. Nanotechnol Rev. 2019;8(1):396–404.

[46] Hayakawa S, Li YX, Tsuru K, Osaka A, Fujii E, Kawabata K. Preparation of nanometer-scale rod array of hydroxyapatite crystal. Acta Biomater. 2009;5(6):2152–60.
[47] Feng J, Song K, Liang S, Guo X, Jianga Y. Electrical wear of TiB_2 particle-reinforced Cu and Cu-Cr composites prepared by vacuum arc melting. Vacuum. 2020;175:109295.
[48] Muthukumar T, Sreekumar G, Sastry TP, Chamundeeswari M. Collagen as a potential biomaterial in biomedical applications. Rev Adv Mater Sci. 2018;53(1):29–39.
[49] Zhang Y, Volinsky AA, Tran H, Chai Z, Liu P, Tian BH, et al. Aging behavior and precipitates analysis of the Cu-Cr-Zr-Ce alloy. Mater Sci and Eng A. 2016;650(1):248–53.